JGR Oceans

RESEARCH ARTICLE

10.1029/2024JC022130

# Observations of Breaking Wave Dissipation and Their Relationship to Atmosphere-Ocean Energy Transfer

**L. Hogan[1], C. J. Zappa[1], A. Cifuentes-Lorenzen[2], J. B. Edson[3], J. O'Donnell[2], and D. S. Ullman[4]**

[1]Lamont Doherty Earth Observatory and Columbia University, Palisades, NY, USA, [2]University of Connecticut, Groton, CT, USA, [3]Woods Hole Oceanographic Institute, Woods Hole, MA, USA, [4]University of Rhode Island, Narragansett, RI, USA

**Key Points:**

- Visible imagery is analyzed to estimate the energy dissipation by breaking waves
- There is agreement between energy input from wind, dissipation by breaking waves, and turbulent dissipation in near-surface ocean
- In mature seas, subsurface dissipation exceeds breaking wave dissipation, implying that additional sources of turbulence are non-negligible

**Correspondence to:**

L. Hogan and C. J. Zappa,
lhogan@ldeo.columbia.edu;
zappa@ldeo.columbia.edu

**Citation:**

Hogan, L., Zappa, C. J., Cifuentes-Lorenzen, A., Edson, J. B., O'Donnell, J., & Ullman, D. S. (2025). Observations of breaking wave dissipation and their relationship to atmosphere-ocean energy transfer. *Journal of Geophysical Research: Oceans*, *130*, e2024JC022130. https://doi.org/10.1029/2024JC022130

Received 15 NOV 2024
Accepted 27 MAY 2025

**Author Contributions:**

**Conceptualization:** C. J. Zappa, D. S. Ullman
**Data curation:** L. Hogan, A. Cifuentes-Lorenzen, J. B. Edson, D. S. Ullman
**Formal analysis:** L. Hogan, C. J. Zappa, A. Cifuentes-Lorenzen, J. O'Donnell, D. S. Ullman
**Funding acquisition:** C. J. Zappa, A. Cifuentes-Lorenzen, J. B. Edson, J. O'Donnell, D. S. Ullman
**Investigation:** C. J. Zappa, A. Cifuentes-Lorenzen, J. B. Edson, J. O'Donnell, D. S. Ullman
**Methodology:** L. Hogan, C. J. Zappa, A. Cifuentes-Lorenzen, J. B. Edson, J. O'Donnell, D. S. Ullman
**Project administration:** C. J. Zappa, A. Cifuentes-Lorenzen



**Abstract** Energy is transferred from the atmosphere to the ocean primarily through ocean surface waves, and the majority is dissipated locally in the near-surface ocean. Observations of turbulent kinetic energy (TKE) in the upper ocean have shown dissipation rates exceeding law-of-the-wall theory by an order of magnitude. The excess near-surface ocean TKE dissipation rate is thought to be driven primarily by wave breaking, which limits wave growth and transfers energy from the surface wave field to the wave-affected layer of the ocean. Here, the statistical properties of breaking wave dynamics in a coastal area are extracted from visible imagery and used to estimate TKE dissipation rates due to breaking waves. The statistical properties of whitecap dynamics are quantified with $\Lambda(c)$, a distribution of total whitecap crest length per unit area as a function of crest speed, and used to compute energy dissipation by breaking waves, $S_{ds}$. $S_{ds}$ approximately balances elevated subsurface dissipation in young seas but accounts for only a fraction of subsurface dissipation in older seas. The wind energy input is estimated from wave spectra from polarimetric imagery and laser altimetry. $S_{ds}$ balances the wind energy input except under high winds. $\Lambda(c)$-derived estimates of TKE dissipation rates by breaking waves compare well with the atmospheric deficit in TKE dissipation, a measure of energy input to the wave field (Cifuentes-Lorenzen et al., 2024). These results tie the observed atmospheric dissipation deficit and enhancement in subsurface TKE dissipation to wave driven energy transport, constraining the TKE dissipation budget near the air-sea interface.

**Plain Language Summary** Video imagery of the sea surface is analyzed to derive breaking wave statistics. Breaking waves dissipate wave energy and inject turbulent energy into the near-surface ocean. We compare the estimates of energy dissipation by breaking waves to estimates of wind energy going into wave growth and find that under weak to moderate winds, energy dissipation by breaking waves balances wind energy input. Under high winds, wind energy input exceeds energy dissipation, and wave growth is inferred. Energy dissipation by breaking waves is also compared to measurements of turbulent energy in the near-surface ocean. Although breaking waves are responsible for most of the subsurface turbulence in strongly forced conditions (high winds, many breaking waves), they account for only a small fraction of subsurface turbulence in weakly forced conditions, indicating the importance of other sources of turbulence.

## 1. Introduction

Ocean surface waves mediate the kinetic energy input to the ocean from the wind. Globally, approximately 70 TW of wind energy goes into the ocean, of which more than an estimated 68 TW goes into surface gravity waves (Rascle et al., 2008; Wunsch, 2020), before being transferred into ocean currents or into turbulent vertical mixing. The primary mechanism by which energy is injected into the upper ocean from surface gravity waves is wave breaking, which dissipates energy from the wave field and enhances turbulence in the ocean mixed layer. On a global scale, the near-surface ocean turbulence and mixing introduced by breaking waves affect the depth of the mixed layer, which has implications for ocean heat uptake, sea surface temperature, and the global carbon budget (Belcher et al., 2012; Sallée et al., 2013). Breaking waves also enhance air-sea gas exchange through bubble-mediated transfer and elevated near-surface turbulence (Brumer et al., 2017; Deike & Melville, 2018; Zappa et al., 2001, 2003, 2007) and generate sea spray, which alters the chemical and radiative properties of the atmospheric boundary layer, accounting for half of all nonanthropogenic aerosols (Veron, 2015) and amplifying sensible and latent heat fluxes (Mulcahy et al., 2008; Veron, 2015).

**Resources:** C. J. Zappa, A. Cifuentes-Lorenzen, J. B. Edson, J. O'Donnell, D. S. Ullman
**Software:** L. Hogan, A. Cifuentes-Lorenzen, D. S. Ullman
**Supervision:** C. J. Zappa
**Visualization:** L. Hogan
**Writing – original draft:** L. Hogan
**Writing – review & editing:** L. Hogan, A. Cifuentes-Lorenzen, J. B. Edson, J. O'Donnell, D. S. Ullman

Here, we focus on the role of breaking waves in limiting wave growth and enhancing turbulence in the near-surface ocean. At the sea surface, the energy balance of the wave field is expressed in the wave action (radiative transfer) equation (e.g., Komen et al., 1994):

$$\frac{\partial}{\partial t}\left(\frac{E}{\omega}\right) + (U + c_g)\cdot\nabla\left(\frac{E}{\omega}\right) = S_{\mathrm{nl}} + S_{\mathrm{in}} - S_{\mathrm{ds}} \tag{1}$$

Here, $E/\omega$ is wave action, the wave energy normalized by frequency. In steady state, assuming no or very slow wave growth ($\partial/\partial t = 0$), this is a balance between the advection of energy through the wave spectrum and three source terms: wind energy input, $S_{\mathrm{in}}$, wave energy dissipation, $S_{\mathrm{ds}}$, and nonlinear wave-wave interactions, $S_{\mathrm{nl}}$. Observations show that energy flux divergence and nonlinear wave-wave interactions are of equal and opposite sign (Romero et al., 2012). Therefore, when spectrally integrated, there is a first order balance between wind input and dissipation:

$$S_{\mathrm{in}} - S_{ds} \cong 0 \tag{2}$$

Dissipation is primarily done by wave breaking, which limits wave growth and transfers wind energy to the ocean.

Phillips' (1985) spectral framework on breaking waves defines a crest length distribution, $\Lambda(c)$, as the total breaking crest length per unit sea surface area propagating at a speed in the range $c$ to $c + dc$. This framework, effectively a histogram of both length and velocity (Jessup & Phadnis, 2005), quantifies wave breaking with velocity scale dependence. Laboratory measurements of energy loss by breaking waves produced by a towed hydrofoil show the energy loss per unit length of breaking wave to be proportional to $\rho b c^5 g^{-1}$, where $b$ is a numerical coefficient of breaking strength, $\rho$ is the density of water, and $g$ is the gravitational constant (Duncan, 1981). Though the laboratory case of a standing wave breaking over a towed hydrofoil is not a direct analogy for the unstable intermittent breaking of ocean waves, Phillips assumes that this scaling will hold in ocean waves and relates this energy loss relationship to the $\Lambda(c)$ framework such that the rate of energy loss by breaking waves with velocities in the range in the range $c$ to $c + dc$ is

$$S_{\mathrm{ds}}(c) = \rho b g^{-1} c^5 \Lambda(c) \tag{3}$$

or the rate of total energy loss per unit sea surface area by breaking waves of any velocity is

$$S_{\mathrm{ds}} = \rho b g^{-1} \int c^5 \Lambda(c)\, dc \tag{4}$$

and the rate of momentum transfer from the wave field by breaking waves is

$$M = \rho b g^{-1} \int c^4 \Lambda(c)\, dc \tag{5}$$

Phillips (1985) predicts the theoretical form of $\Lambda(c)$ in the equilibrium subrange, where $S_{\mathrm{ds}} = S_{\mathrm{in}}$: assuming a wave spectrum of the form $\Psi(k) \propto k^{-5/2}$, he predicts that $S_{\mathrm{in}}$ and $S_{\mathrm{ds}}$ both decay as $c^{-1}$. If $S_{\mathrm{ds}}$ has the form $S_{\mathrm{ds}} \propto c^{-1}$, then following Equation 4, the crest length distribution should decay as $\Lambda(c) \propto c^{-6}$ in the equilibrium range. The shape of $\Lambda(c)$ decays by $c^{-6}$ as expected by theory of the equilibrium range in both observations (Melville & Matusov, 2002; Schwendeman et al., 2014) and numerical simulations (Wu et al., 2023) though not for all wind or wave conditions (Gemmrich et al., 2013; Kleiss & Melville, 2010). The shape of $\Lambda(c)$ is sensitive to wind and wave conditions and has been found to collapse with various scaling arguments based on wind speed (Melville & Matusov, 2002), friction velocity, wave speed, wave height, (Deike & Melville, 2018; Sutherland & Melville, 2013), and fetch (Kleiss & Melville, 2010). Implementing a $\Lambda(c)$-based dissipation term in the WaveWatchIII model replicates observed dissipation rates and improves the accuracy of the spectral shape in model output (Romero, 2019).

Observations of breaking waves are often done with visible imagery and are therefore limited to whitecaps, or breaking waves that entrain bubbles and therefore have a visible signature on the sea surface (Eadi Stringari

et al., 2021; Gemmrich et al., 2008, 2013; Kleiss & Melville, 2010; Melville & Matusov, 2002; Schwendeman & Thomson, 2015; Thomson & Jessup, 2009; VreĆica et al., 2022). Infrared imagery has been applied to observe both whitecaps and microscale breaking waves ("microbreakers") that do not entrain air and therefore have no visible signature (Jessup et al., 1997; Jessup & Phadnis, 2005; Sutherland & Melville, 2013), and observations suggest that the impact of microbreakers on $S_{ds}$ is small with magnitude within the uncertainty of estimates relying solely on visible imagery (Sutherland & Melville, 2015). In the context of energy dissipation, although Sutherland and Melville (2015) find that microbreakers contribute a large fraction of energy dissipation by breaking waves, particularly in old seas, they support only a small fraction of subsurface turbulent kinetic energy (TKE) dissipation (Banner & Morison, 2018).

Breaking waves impact the structure of turbulence in the ocean in a thin layer at the surface. Under no breaking, the structure of turbulence could be inferred from the law of the wall (LOW), treating the ocean surface as a rigid, flat boundary, such that the shear flow is given by

$$\partial U/\partial z = u_*/\kappa z \tag{6}$$

Where $u_*$ is the water-side friction velocity, $z$ is the depth (distance) from the boundary, and $\kappa$ is von Karman's constant. In terms of the TKE balance for a steady state under horizontally homogeneous and neutral conditions (i.e., negligible buoyancy flux) shear dominates TKE production. For a constant stress layer, the profile of dissipation should be determined by the profile of $\partial U/\partial z$, and the profile of $\varepsilon$ in the surface ocean layer by LOW is:

$$\varepsilon = -\frac{\partial U}{\partial z}[\langle u'w'\rangle] = \frac{u_*^3}{\kappa z} \tag{7}$$

where $\varepsilon$ decays with depth as $z^{-1}$. However, near-surface observations show $\varepsilon$ to be an order of magnitude greater than the LOW prediction, an excess attributed to breaking waves (Agrawal et al., 1992; Craig & Banner, 1994; Drennan et al., 1992; Terray et al., 1996; Toba & Kawamura, 1996). Mechanistically, elevated dissipation driven by wave breaking is temporally and spatially intermittent (Agrawal et al., 1992) and linked to a "downward bursting" of flow (Toba & Kawamura, 1996) with a near-surface magnitude equal to observed and modeled wind energy input (Craig & Banner, 1994; Drennan et al., 1992; Terray et al., 1996).

Terray et al. (1996) and Drennan et al. (1992) propose a conceptual framework for subsurface dissipation profiles in which three layers are defined: the breaking layer in which turbulence is generated by breaking waves and $\varepsilon$ is elevated and assumed constant in order to balance kinetic energy flux from breaking waves. In the "wave-affected layer," vertical transport of TKE from the breaking layer is balanced by dissipation resulting in a profile deviating from LOW as $z^{\gamma}$ with $\gamma = -2$ and a lower layer in which the dominant TKE balance is between shear production and dissipation, where the dissipation profile follows LOW, leading to $\gamma \approx -1$. Many observations support this conceptual model for near-surface $\varepsilon$ (Drennan et al., 1996; Gerbi et al., 2009; Sutherland & Melville, 2015; Thomson, 2012), though observations in seas with a mix of swell and wind waves do not follow the predicted scaling (Sutherland et al., 2013). Other studies have found similar profiles, such as a profile with $\gamma = -2$ below one significant wave height and $\gamma = -1$ closer to the surface (Sutherland & Melville, 2015). Observations of $\varepsilon$ in high wind and strongly breaking conditions find $\gamma$ values of $-1.4\ to\ -1.6$ (Gemmrich, 2010; Thomson et al., 2016; Ticona Rollano et al., 2019). Phase resolved measurements show that the elevated $\varepsilon$ over LOW is limited to the crests of waves, where it is 1.6 times greater than wave troughs with $\gamma = -2.3$ above the mean water level (Gemmrich & Farmer, 2004), and the profile of $\varepsilon$, or the value of $\gamma$, depends on the reference height (Gemmrich, 2010). Below the wave-affected layer, the $\varepsilon$ is not affected by wind-wave produced turbulence. In cases of very weak wind forcing, where buoyancy dominates, $\varepsilon$ is well described to greater depth by a function of buoyancy flux and law of the wall (Miller et al., 2023). Langmuir turbulence is also important at greater depths, where downwelling jets from orbital velocities of long waves impact the structure of turbulence at the bottom of the mixed layer (Belcher et al., 2012; Li & Fox-Kemper, 2017).

Though the excess TKE dissipation in the wave affected layer is understood to be the pressure-driven vertical transport of TKE from breaking waves (Cifuentes-Lorenzen et al., 2024; Scully et al., 2016; Scully & Zippel, 2024), few studies directly link measurements of wave-breaking $S_{ds}$ to the excess dissipation. Additionally,

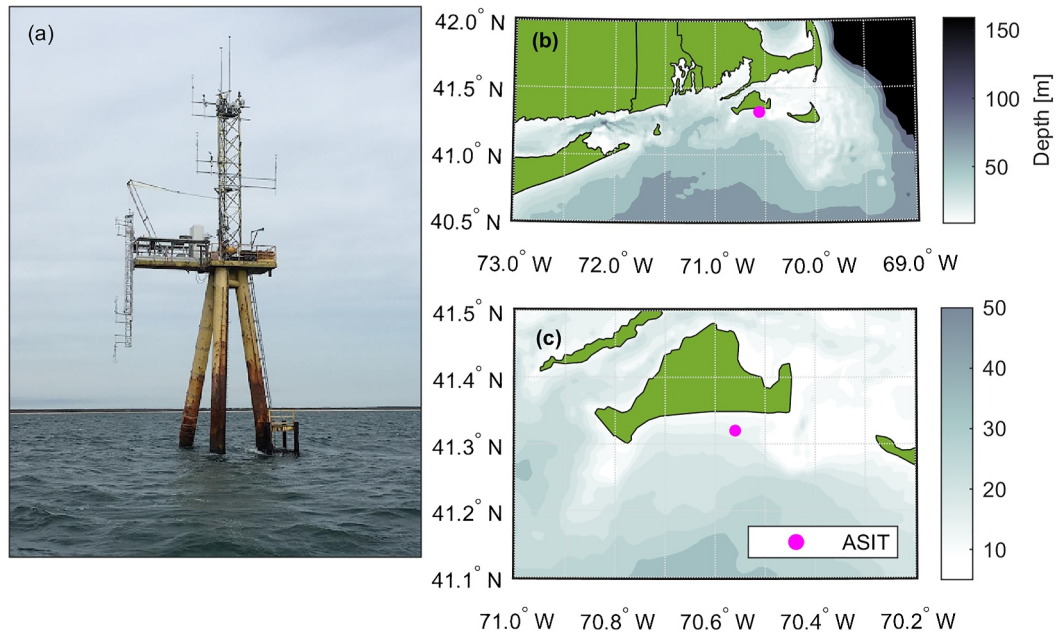


**Figure 1.** Air-sea interaction tower (ASIT) is pictured after installation (a). Maps of ASIT location are shown with bathymetry (depth in meters) indicated in gray colorscale (b, c).

studies that compare $S_{ds}$ from breaking waves to depth-integrated $\epsilon$ identify a narrow range of conditions under which they balance (Sutherland & Melville, 2015; Thomson et al., 2009).

This work specifically aims to relate breaking wave statistics to depth integrated TKE dissipation rates and atmosphere-ocean energy transfer. Observations of breaking waves and wave spectra are used to estimate wave energy source terms and evaluate the theoretical $S_{in}$-$S_{ds}$ balance. $S_{ds}$ by wave breaking is then compared to depth integrated TKE dissipation rates in the uppermost meter of the ocean, assessing to what degree energy from waves is dissipated in the near-surface layer. These estimates of energy flux through the wave field are also compared to the wind energy input estimates from the observed TKE dissipation rate deficit by Cifuentes-Lorenzen et al., 2024. The structure of the paper is as follows: Section 2 describes the air-sea interaction tower (ASIT) TKE field campaign and the methods of estimating $S_{ds}$ from whitecap statistics and $S_{in}$ from wave energy spectra, Section 3 presents and compares estimates of $S_{ds}$ and $S_{in}$ to measurements of excess near-surface TKE dissipation, and Section 4 discusses their relationship to air-sea energy transfer and near-surface profile of TKE dissipation.

## 2. Methods

### 2.1. ASIT 2019 TKE Campaign

The ASIT TKE experiment was conducted between October 2019 and February 2020 from the ASIT (Figure 1a), approximately 3 km off the coast of Martha's Vineyard, MA (Figure 1b), with the goal of quantifying the TKE budget above and below the air-sea interface, including the effects of waves and currents on the sea surface. The tower was equipped with an array of sonic anemometers, positioned between 4 and 22 m above mean sea level, for measuring vertical profiles of wind velocities and turbulent fluctuations. A triplet of laser altimeters, two visible cameras, an infrared camera, and a polarimetric imager captured the wave conditions of the sea surface. Nearby, a mooring of CTDs (SeaBird Microcat) and ADCPs (Nortek Aquadopp, Nortek Signature 1,000 kHz, and RDI Sentinel 1,200 kHz) measured profiles of temperature, salinity, turbulent velocities, currents, and two-dimensional wave spectra in 19 m water depth. TKE dissipation rate estimates in the near surface were derived from an Aquadopp mounted on a small spar buoy, allowing for near-surface measurements in a wave-following reference between 1.1 m up to approximately 0.3 m below the surface (Cifuentes-Lorenzen et al., 2024).

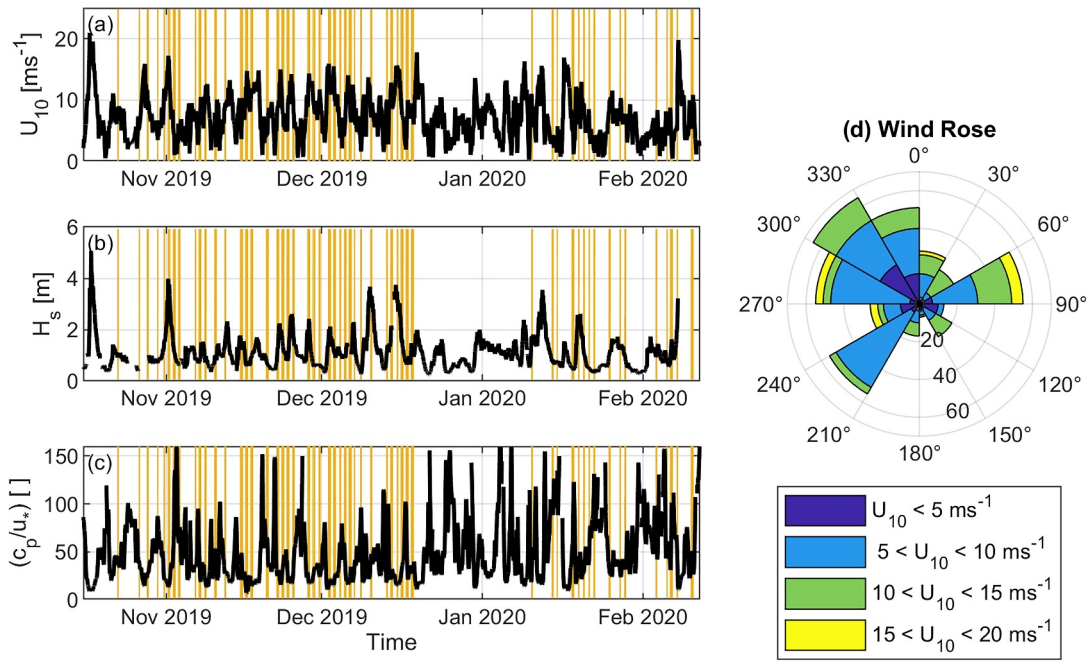


**Figure 2.** Time series of (a) wind speed, (b) significant wave height, and (c) wave age with recording times of the Imperx visible cameras highlighted in yellow, (d) Wind rose (following meteorological convention of direction from in degrees clockwise from North) for each Imperx visible camera acquisition.

The focus of this paper is the analysis of visible imagery from the pair of visible cameras mounted on ASIT. Two monochromatic video cameras (Imperx Lynx), with sensing arrays of 992 × 992 pixels, captured video of the sea surface at a 20 Hz frame rate in 20-min intervals each hour throughout daylight hours. Wide angle lenses captured large swaths of the sea surface (approximately 2,580 m$^2$) to observe whitecaps. In total, 660 20-min recordings were taken of which 365 were discarded for poor light conditions, resulting in 295 segments for analysis. Polarimetric imagery was taken with a visible polarimetric camera (Polaris Pyxis Mono Vis) with a 2,464 × 2,056 (4 megapixel) sensing array and a field of view of approximately 9 m$^2$. Polarimetric imagery was recorded at a 30 Hz frame rate in 10-min intervals each hour throughout daylight hours. In total 307 10-min recordings were taken of which 193 segments were of sufficient quality for spectral analysis.

The instruments were deployed for nearly 6 months, producing a data set that spans a large parameter space of wind and wave conditions. The 10-m wind speed, $U_{10}$, frequently reached 15 ms$^{-1}$ (Figure 2a). ASIT is positioned due south of an east-west oriented coastline, as shown in Figure 1, allowing for comparison of onshore and offshore wind conditions. Offshore winds (short-fetch winds from the north) and onshore winds (unlimited-fetch winds from the south) were observed at most wind speeds (Figure 2d). The significant wave height, $H_s$, (Figure 2b) varied from 0 to 2 m with storms driving waves of up to 4 m, and wave age varied between developing seas and very old, swell-dominated seas (Figure 2c). Visible imagery of whitecapping captured most of the variability of this data set.

### 2.2. $S_{ds}$: The Initial Velocity Method and $\Lambda(c)$

Whitecaps were identified and tracked in grayscale video of the sea surface. Each image is first corrected for camera intrinsics, of which the wide-angle lens caused moderate distortion of each frame, then orthorectified to account for camera extrinsic properties, including a 40° look angle and a 23 m freeboard height.

Past studies have shown that $\Lambda(c)$ results are sensitive to the whitecap identification and tracking method, such as the "contour method" which identifies whitecap crests from gradient contours in single images, and the "ellipse method" which differences two consecutive images to extract the propagating front of the breaking crest (Kleiss & Melville, 2011). The "element-wise" method treats each whitecap as a combination of small breaking segments (Kleiss & Melville, 2010; Sutherland & Melville, 2013), whereas the "event-wise" method assigns a single speed

and crest length to each whitecap event (Gemmrich et al., 2008), and the Fourier based method of Thomson and Jessup (2009) computes a speed spectrum for all whitecaps in a video segment. Here, we follow the method of Gemmrich et al. (2008, 2013) using the event-wise ellipse method to identify whitecap crest features in the imagery and treating each crest as a single event with one characteristic length and speed.

This method takes the difference between consecutive images to isolate the bright, advancing crests of whitecaps, which appear as high positive values in the differenced images. The differenced images are normalized by their maximum value and binarized with a constant intensity threshold of 0.6, producing binary images where whitecap crest features have pixel values of 1 and all other pixels are 0. A series of image processing steps are done to fill holes in the features before each whitecap crest is identified as a single feature. The MATLAB Image Processing toolbox is used to approximate each whitecap crest feature as an ellipse and calculate its properties, including major axis length, minor axis length, centroid position, area, and orientation. Crests are matched from one frame to the next based on differences in centroid position, area, and orientation. The crest length distribution, $\Lambda(c_b)$, is calculated as

$$\Lambda(c_b) = \frac{L_b t_b}{T\, A\, \Delta c_b} \tag{8}$$

$L_b$ is the breaking crest length, $t_b$ is the duration of the breaking event, $T$ is the total duration of video segment, $A$ is the total area of sea surface captured by the image, and $\Delta c_b$ is the breaker speed bandwidth ($\Delta c_b = 0.2\ \mathrm{ms}^{-1}$). Each event is assigned one length $L_b$, defined as the maximum length of the major axis recorded throughout the breaking event. The duration of each breaking event, $t_b$, is defined as the frame rate multiplied by the number of frames for which the whitecap is tracked. The image processing algorithm tracks each whitecap object until the propagation direction changes by more than 90°, indicating that the object is no longer an actively breaking whitecap but instead is residual foam passively advected by long wave orbital motion.

The initial speed of a whitecap crest, $c_b$, is slower than the underlying phase speed $c_b < c$ and the crest speed decreases over the course of a breaking event (Banner, Barthelemy, et al., 2014, Banner, Zappa, & Gemmrich, 2014). Though the crest speed varies, each breaking event is assigned one value, $c_b$, corresponding to the initial velocity. This preserves the spectral nature of the Phillips-Duncan framework, in which breaker speed stands in for wavenumber and defines the scale of the event. Following Gemmrich et al. (2013), the propagation speed of a given crest is calculated for each time step of the event, a linear function is fit to the time series of $c_b$ over the event, and $c_b$ is defined as the value of the linear fit at the first time step. This definition for $c_b$ approximates the phase speed of the underlying wave as it begins to break, taking into account the decay of $c_b$ over the course of a breaking event. The total translational centroid displacement is used to define crest speed, following Gemmrich et al. (2008) and the analysis of Kleiss and Melville (2011). The tracking algorithm requires a set maximum centroid displacement, beyond which two crests in consecutive frames are labeled as separate events, rather than matching them as a single crest. The propagation speed is the total displacement of the centroid of the ellipse multiplied by the frame rate, 20 Hz, and therefore the displacement threshold sets a maximum propagation speed. The maximum displacement is set to 100 pixels, corresponding to a maximum $c_b = 14\ \mathrm{ms}^{-1}$. Once $c_b$ has been computed from the imagery, it is related to the phase speed of the underlying wave, $c$, with $c = \alpha c_b$. Laboratory measurements (Rapp & Melville, 1990; Stansell & MacFarlane, 2002) and modeling studies (Banner, Barthelemy, et al., 2014, Banner, Zappa, & Gemmrich, 2014) have found $\alpha$ in the range [0.7–0.9]. Here, $c_b$ is translated to $c$ with a value of $\alpha = 0.8$.

### 2.3. ϵ: Near-Surface Dissipation

Subsurface TKE dissipation is computed from Aquadopp measurements with the centered-difference turbulence structure function method of (Wiles et al. (2006) and Gemmrich and Farmer (2004) and validated with the spectral method of (Zippel et al., 2021). From the Aquadopp attached to the spar buoy, a subsurface dissipation profile was fit to the data between $z = [-1.10,\ -0.32]$ m. Following Terray et al. (1996), a constant layer of dissipation is assumed close to the surface. However, although Terray et al. (1996) assume a constant layer from $z/H_s = -0.6$, measurements from the Aquadopp are resolved beyond that, and the constant layer is assumed between $z = -0.32$ m and the surface (i.e., $z/H_s \sim 0.27$). Total near-surface dissipation is integrated as

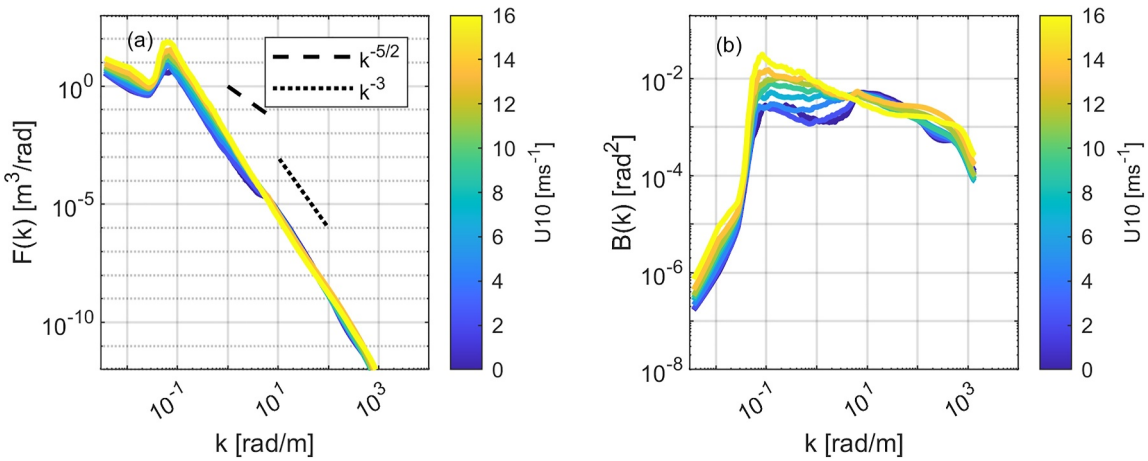


**Figure 3.** Wave Height (a) and Saturation (b) spectra computed from the LiDAR altimeter and polarimetric camera.

$$\epsilon_{\text{spar}} = \int_{-1.1}^{-0.3} \epsilon(z)\, dz + \left(\epsilon_{z=-0.32} \times 0.32\text{m}\right) \tag{9}$$

Here, the subsurface dissipation measurements presented have previously been described by Cifuentes-Lorenzen et al. (2024).

### 2.4. $S_{in}$: Spectral Estimate for Wind Energy Input

The wind energy input is estimated with parameterizations of the wave growth rate and measured wave spectra. To construct full wave spectra, the wave height spectra from the LiDAR altimeters were combined with the wave slope spectra retrieved with the polarimetric camera. The wave height spectrum, $\Psi(\text{k})$, computed from the LiDAR altimeters captures low wavenumber waves ($k = 0.0004 - 4\,\text{rad}\,\text{m}^{-1}$). Small-scale waves ($k = 2 - 1400\,\text{rad}\,\text{m}^{-1}$) are measured with the polarimetric camera, which captures high spatial resolution imagery with O (1 mm) pixel scale. The polarimetric slope sensing technique (Zappa et al., 2008) is used to reconstruct the sea surface slope field. From the slope field, the wavenumber-frequency slope spectrum $S(k_x, k_y, f)$ is integrated over frequency and direction and multiplied by $k^2$ to yield the wave height spectrum, $\Psi(\text{k})$. Figure 3 shows wave height, slope, and saturation spectra of the combined LiDAR-polarimetry measurements, with lines indicating slopes of $k^{-5/2}$ and $k^{-3}$, indicating behavior of the equilibrium and saturation ranges. Although the LiDAR ran constantly over the measurement period, the polarimetric camera only recorded intermittently. To fill in the high wavenumber spectra for instances when the polarimetric camera was not running, the existing polarimetry-derived spectra were binned according to the friction velocity, $u_*$, and the mean spectrum for the given $u_*$ condition filled missing data.

The combined spectra from the polarimeter and laser altimeters are used to estimate the wind energy input term, $S_{\text{in}}$ (e.g., Donelan et al., 2006):

$$S_{\text{in}} = \rho_w g \int \beta(k) \cos(\theta)\, \Psi(k)\, dk \tag{10}$$

where $k$ is the radian wavenumber, and $\cos(\theta)$ accounts for misaligned wind and waves. The wave spectra in this data set lack directional information in the wavenumber range $k = 0.004 - 4$ rad m$^{-1}$. It is assumed that the angle between the wind and the waves is small (consistent with observations by Plant, 1982; and noted by Phillips, 1985) and therefore the $\cos(\theta)$ term is neglected. $\beta$ is a wave growth rate, parameterized by Plant (1982), and Donelan and Pierson (1987), respectively:

$$\beta = 0.04 \left(\frac{u_*}{c}\right)^2 \omega \tag{11}$$

$$\beta = 0.194\ \frac{\rho_a}{\rho_w}\left(\frac{\mathrm{u}_{\lambda\backslash 2}}{\mathrm{c}} - 1\right)^2 \omega \tag{12}$$

Here, $\mathrm{u}_{\lambda\backslash}$ is the wind speed at a height of one-half of the wavelength.

In addition to the three parameterizations that compute $S_{\mathrm{in}}$ with these spectra and empirical wave growth parameters, $S_{\mathrm{in}}$ is also estimated with the functions of water-side stress, $u_{*w}^2$, by Phillips (1985) and Gemmrich et al. (1994):

$$S_{\mathrm{in}} = \chi u_{*w}^3 \ln\left(\frac{k_1}{k_0}\right) \tag{13}$$

$$S_{\mathrm{in}} = \rho_w\, c_e\, u_{*w}^2 \tag{14}$$

In Equation 13, $S_{\mathrm{in}}$ is related to $u_{*w}^3$, a constant, $\chi$ ($\chi$ represents a series of constants from Phillips (1985) specified as approximately $10^{-3}$), and a range of wavenumbers bounding the equilibrium range, that is $k_0 = 2k_p$ and $k_1 = g/u_*^2$. Equation 14 relates stress ($u_{*w}^2$) to the energy input with $c_e$, a wave-related velocity, defined as the mean wave speed supporting momentum transfer in fully rough flow where shear stress can be neglected. In equilibrium, $c_e = S_{\mathrm{ds}}/\tau$, where $\tau = \rho u_*^2$ is the stress. Prior observations have found $c_e = 1 - 2\ \mathrm{ms}^{-1}$ (Gemmrich et al., 1994, 2008; Thomson et al., 2016). Here, by computing both $c_e = S_{\mathrm{ds}}/\rho u_*^2$ and $c_e = \int c^5 \Lambda(c)\, dc / \int c^4 \Lambda(c)\, dc$, a mean value of $c_e = 4.3\ \mathrm{ms}^{-1}$ is determined from the ASIT data set. Though higher than previously reported values, the ratio $c_e/c_p$ for the ASIT data set is 0.5 similar to the value reported by Terray et al. (1996). We interpret this higher value for $c_e$ as due to a data set representative of more mixed and old seas. Additionally, $c_e$ is computed by limiting the bounds of integration of $\int c^5 \Lambda(c)\, dc / \int c^4 \Lambda(c)\, dc$ to $c < c_p$, which results in a mean value of $c_e = 1.9\ \mathrm{ms}^{-1}$, indicating that approximately half of the energy input to the wavefield is supported by wave scales larger than the spectral peak. This lower value of $c_e$, representative of waves at scales smaller that the spectral peak, is closer to previously reported values and closer to the ratio $c_e/c_p = 0.2\ \mathrm{ms}^{-1}$ reported by Thomson et al. (2016). Below, a range of $S_{\mathrm{in}}$ values computed from Equation 14 are presented, reflecting a range of $c_e = 1.9 - 4.3\ \mathrm{ms}^{-1}$. A comparison of $S_{\mathrm{in}}$ from these parameterizations and $S_{\mathrm{ds}}$ from wave breaking evaluates the assumption that dissipation by wave breaking balances wind energy input.

## 3. Results

$\Lambda(c)$ computed from the IVM method of whitecap identification and tracking are shown in Figure 4. Consistent with previous results using visible imagery, the distributions peak at breaker speeds around 2-5 $\mathrm{ms}^{-1}$ and decay around the expected shape of $\mathrm{c}^{-6}$ (Gemmrich et al., 2008; Kleiss & Melville, 2010). More breaking occurs at higher wind speeds across all scales, but most notably at high crest velocities (Figure 4), which is critical to energy dissipation. Across all breaking velocities, $\Lambda(c)$ is inversely related to wave age, which is consistent with results of previous studies (Deike & Melville, 2018; J. Gemmrich et al., 2013; Kleiss & Melville, 2010).

Dissipation is strongly impacted by the shape of $\Lambda(c)$ at high speeds, where the scaling $c^5$ is very large. Though the shape of $\Lambda(c)$ for high speed crests deviates from the expected $c^{-6}$ decay and appears to level off, this behavior is consistent with prior results (Gemmrich et al., 2013; Kleiss & Melville, 2010). This behavior at high breaker speeds is consistent when the parameters of the whitecap identification method are varied: for instance, there is no change in high breaker speed shape when the maximum possible speed is doubled. Previous studies have also shown that this behavior is consistent among various processing methods (Kleiss & Melville, 2011). A few large-scale breaking waves cause the shape of $\Lambda(c)$ to deviate from $c^{-6}$. To test the sensitivity of $S_{\mathrm{ds}}$ to these few large-scale breaking waves, we alter the shape of $\Lambda(c)$ to follow $c^{-6}$ out to $c_{\mathrm{max}}$ where $c_{\mathrm{max}}$ is the maximum speed of a wave resolved by the whitecap identification algorithm within the 20-min video sequence. These extensions are shown in the dotted lines in Figure 4. The impact of these large-scale breakers on $S_{\mathrm{ds}}$ is discussed below.

The results of Sutherland and Melville (2013) show that small-scale, slow microbreakers, though not captured by visible imagery, impact dissipation estimates. They show that $\Lambda(c)$ does not roll off below the range of peak breaking speed found in prior visible imagery studies (2-5 $\mathrm{ms}^{-1}$), and instead infrared imagery shows a roll off

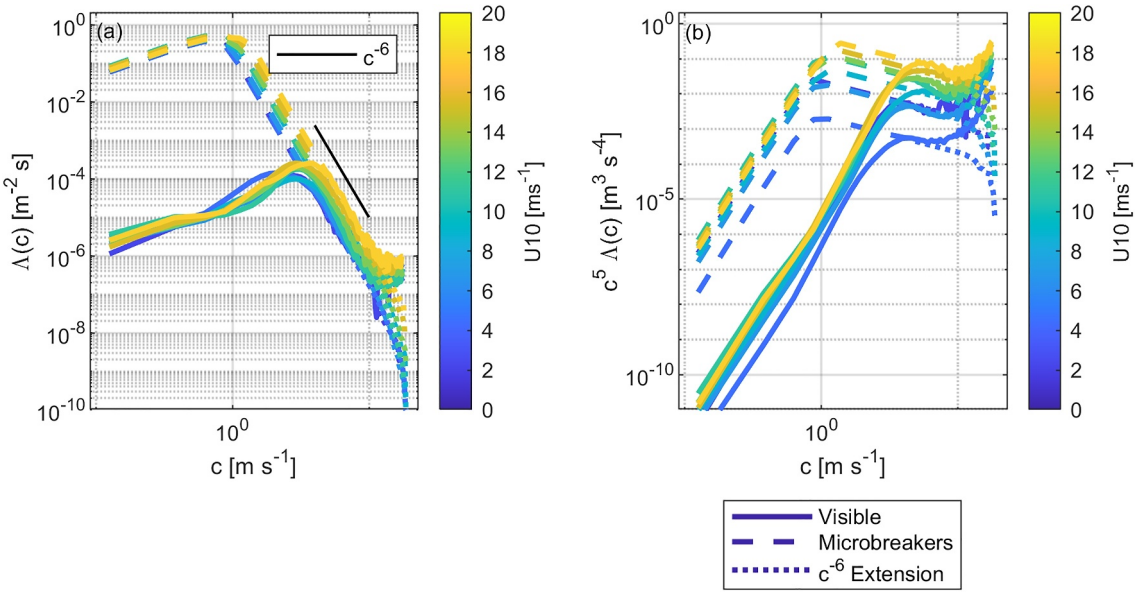


**Figure 4.** $\Lambda(c)$ (a) and $S_{ds}(c)$ (b) colored by wind speed. $\Lambda(c)$ and $S_{ds}(c)$ computed from visible imagery is shown in solid lines, whereas extensions to account for microbreaking are shown in dashed lines, and extensions following $c^{-6}$ are shown in dotted lines. The black line in (a) represent the theoretical decay of $c^{-6}$ expected by the Phillips-Duncan framework.

closer to 0.2 $ms^{-1}$, where $\Lambda(c)$ reaches a peak of approximately 1 $m^{-2}s$. To consider the impact of microbreakers, we append a low-speed distribution to the results of the visible imagery analysis shown in the dashed lines of Figure 4. This extends $\Lambda(c)$ from just past the original peak to an upper limit of $\Lambda(c) = 1\ m^{-2}s$, following a $c^{-6}$ decay, and rolls off at speeds below that. This results in distributions that peak 0.5–0.9 $ms^{-1}$, the effect of which on $S_{ds}$ is discussed below.

To estimate $S_{ds}$ from $\Lambda(c)$, a unitless breaking strength parameter, $b$, is required. Though initially considered a constant (Duncan, 1981; Phillips, 1985), laboratory and field observations have shown that $b$ varies over orders of magnitude (see Romero et al., 2012 Figure 1 and citations therein). However, applying a scale dependence to $b$ within the $\Lambda(c)$ framework alters the $c^5$ scaling which underpins the framework. For estimating $S_{ds}$ by broadband breaking, it is useful to compute the effective breaking strength, $b_{eff}$, as a factor that equates subsurface energy dissipation ($\varepsilon$) to the quantity $\Lambda(c)$:

$$b_{eff} = \varepsilon / \left[ \rho g^{-1} \int_c c^5 \Lambda(c)\, dc \right] \tag{15}$$

(Zappa et al., 2016, hereafter Z2016) leveraged three observational data sets and three existing models for $b$ and parameterized $b_{eff}$ as a function of wave age. Romero et al. (2012, hereafter R2012) model $b$ spectrally as a function of the wave saturation spectrum, such that $b$ is scale dependent. Here, we compute $S_{ds}$ with the Z2016 parameterization:

$$b_{Z16} = A + B(c_p/u_*) \tag{16}$$

(where $A = 3.482 \times 10^{-3}$ and $B = -4.691 \times 10^{-5}$), and compute $S_{ds}$ with the R2012 parameterization with the measured saturation spectra (Figure 5b):

$$b_{R12}(k) = \left[ A_1 B(k)^{0.5} - B_T(k)^{0.5} \right]^{\frac{5}{2}} \tag{17}$$

(where $A_1 = 4$ and $B_T = 10.2 \times 10^{-4}$). In order to situate the data set within past parameterizations of $b$, $b_{eff}$ is computed with Equation 15 using subsurface measurements of dissipation from the top 1.5 m of the water column. Figure 5 shows the Z2016 parameterization, the R2012 parameterization computed with measured saturation spectra (averaged with respect to wavenumber to be scale independent), and $b_{eff}$ computed with Equation 15

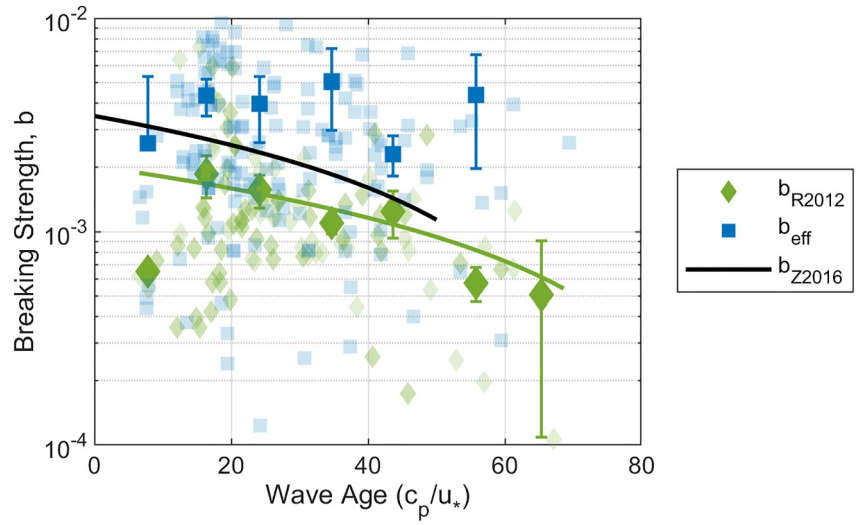


**Figure 5.** Breaking strength parameter, $b$, computed with R2012 parameterization (Equation 17, green), and computed with subsurface dissipation data (Equation 15, blue). Dark symbols with uncertainty bars indicate bin averages (logarithmic mean), and transparent symbols indicate individual datapoints. Uncertainty bars show 95% confidence intervals. The black curve is the Z2016 parameterization for $b$ as a function of wave age, and the green curve is a linear fit to the bin averages of the R2012 parameterization for $b$.

(Figure 5). The effective breaking strength, $b_{eff}$, is significantly higher than the other parameterizations. The R2012 coefficient, $b_{R12}$, compares well with $b_{Z16}$, and a linear function of wave age fit to bins with >10 datapoints yields a function similar to that of $b_{Z16}$, with $A = 2.027 \times 10^{-3}$ and $B = -2.166 \times 10^{-5}$. $S_{ds}$ is computed below using the wavenumber-averaged R2012 model with the saturation spectrum measurements presented in Figure 4, which maintains the $S_{ds} \propto c^5$ scaling of the Phillips-Duncan framework.

Total $S_{ds}$ by breaking waves is computed with Equation 4 and shown in Figure 6, for the original distributions (diamonds), the distributions extended to include microbreaking (circles), and the distributions extended along $c^{-6}$ at high speeds (squares). Under most conditions, estimates of $S_{ds}$ with the removal of large-scale breakers (such that $\Lambda(c)$ follows $c^{-6}$) are within the observed variability of the original distributions. Under weak offshore winds, the

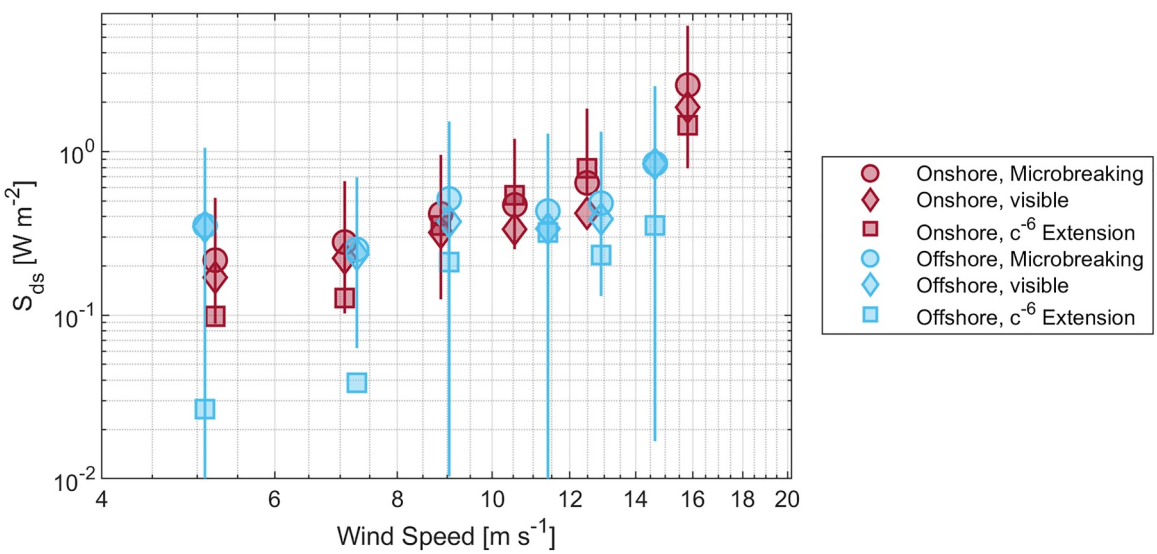


**Figure 6.** $S_{ds}$ in offshore wind (±60° from N) and onshore wind (±60° from S) conditions. $S_{ds}$ computed from $\Lambda(c)$ of visible imagery (diamonds) is shown with $S_{ds}$ computed from microbreaking extensions at low $c$ (circles) and with $S_{ds}$ computed from $c^{-6}$ extensions at high $c$ (squares). Logarithmic means are shown for wind speed (bins of width 2 ms$^{-1}$). 95% confidence intervals are represented with uncertainty bars.

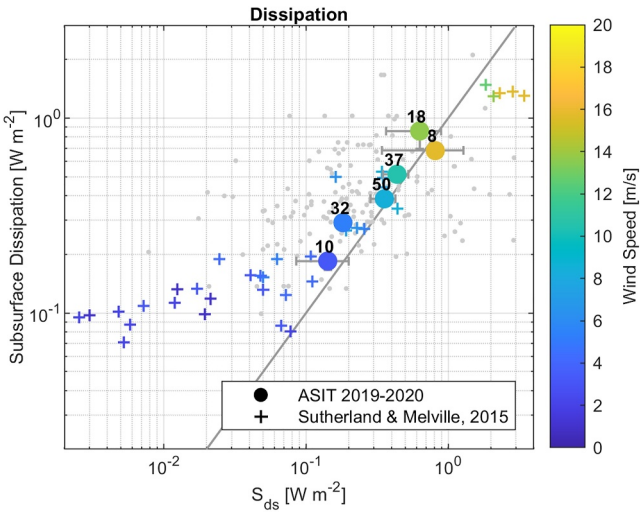


**Figure 7.** $S_{ds}$ from breaking waves and integrated subsurface dissipation from the ADCP on the spar buoy, based on a depth integration in the 1.4 m of the water column, colored by wind speed. Individual datapoints from the 2019 air-sea interaction tower (ASIT) turbulent kinetic energy (TKE) campaign are shown in gray, colored circles are log-mean bin averages for wind speed bins of width 3 $ms^{-1}$ from the 2019 ASIT TKE campaign, and colored crosses are the data from Sutherland and Melville (2015).

removal of these large-scale breakers results in estimates of $S_{ds}$ which fall outside the observed variability of the original distributions. Under these conditions, we expect non-local swell propagating toward the shore against the offshore winds. These conditions would not be in equilibrium, and the assumptions of Phillips (1985) underpinning the $c^{-6}$ scaling argument would no longer hold. Microbreaking increases $S_{ds}$ by approximately 30% (mean of 37% and median of 27%). In 13 cases, microbreaking is greater than twice the estimate of $S_{ds}$. Estimates of $S_{ds}$ from visible imagery is shown in unfilled markers and $S_{ds}$ including the extension for microbreaking in filled markers in Figure 6. Data are shown as the logarithmic mean for wind speed or wave age bins, and the uncertainty bars represent the 95% confidence interval. In general, $S_{ds}$ is greater under stronger wind forcing; however, the role of wind direction is more variable. There is more variability in $S_{ds}$ under offshore winds, likely reflecting misalignment between onshore propagating swell offshore winds (Figure 6).

The well-observed excess in near-surface TKE dissipation is typically attributed to energy from breaking waves. Here, $S_{ds}$ is compared to the TKE dissipation measured over the top 1.4 m of the ocean by the spar buoy referred to here as $\epsilon_{spar}$ (Figure 7). Previously, Cifuentes-Lorenzen et al. (2024) have shown that $\epsilon_{spar}$ balances energy transfer ($S_{in}$ computed with Equations 10 and 11) to first order. When binned by wind speed, the mean breaking wave dissipation and $\epsilon_{spar}$ approximately balance and converge on the 1:1 line. The data from ASIT fall within the range of results presented by Sutherland and Melville (2015, referred to as SM15), who show a similar balance under moderate wind conditions, but also present data in very old seas (wave age > 90), in which subsurface dissipation is much greater than breaking dissipation. This imbalance is further discussed below.

Wind energy input ($S_{in}$) is estimated with measurements of wind stress and the wave spectrum using the empirical parameterizations in Equations 10–14 and shown in Figure 8. Although there is generally good agreement among the parameterizations, at low winds, they vary by nearly an order of magnitude. Functions of the form $a_1(U_{10})^{a_2}$ fit to the observations of $S_{in}$ show that the values of $a_2$ are close to the theoretical scaling of wind energy input as $U^3$. Values of $a_2$ range from 2.8 (Gemmrich et al. (1994) parameterization given by Equation 14) to 3.9 (Phillips (1985) parameterization given by Equation 13). Figure 9 shows a direct comparison of the wave action source terms, $S_{ds}$ and $S_{in}$. Here, $S_{in}$ is shown as the mean of the four parameterizations. Though generally showing good agreement, under high winds and young seas, $S_{in}$ is greater than $S_{ds}$, representing disequilibrium in the wave field.

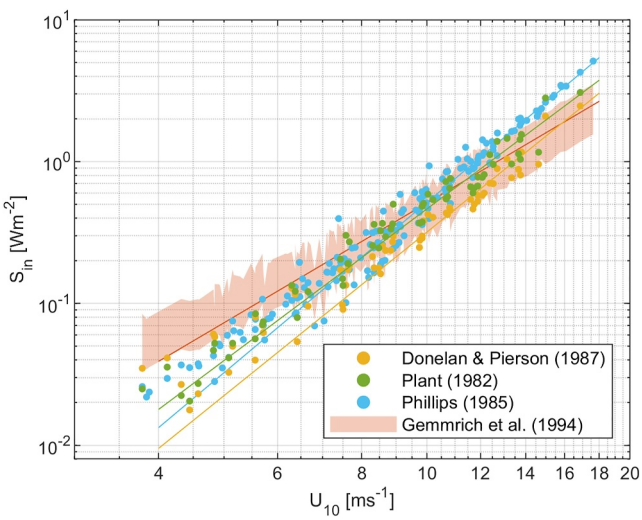


**Figure 8.** $S_{in}$ computed with the parameterizations of Equations 10–14 using observations of wind stress and the wave spectrum are colored by parameterization. Power-law functions fit to the observations are shown. Gemmrich et al. (1994, Equation 14) in orange, Phillips (1985, Equation 13) in blue, Plant (1982, Equations 10 and 11) in yellow, and Donelan and Pierson (1987 Equation 10 and Equation 12) in green. Power fits to the data are shown.

## 4. Discussion

### 4.1. Wave Mediation of Near-Surface Turbulence

Excess near-surface TKE dissipation is often attributed to breaking waves (e.g., Sutherland & Melville, 2015; Terray et al., 1996; Thomson et al., 2009). Independent estimates during our experiment are presented in Figure 7, confirming the role of wave breaking in driving this enhancement, with order of magnitude agreement between $S_{ds}$ and $\epsilon_{spar}$ over a range of wind speeds. However, data presented in Figure 10 as the fraction of subsurface dissipation, $\epsilon_{spar}$, that is accounted by breaking wave dissipation, $S_{ds}$, show variability with wave age with a considerable imbalance in breaking dissipation and subsurface dissipation for high wave ages (old seas). Under these conditions breaking dissipation accounts for less than half of subsurface dissipation at wave ages >50. This is consistent with the results of SM15, who

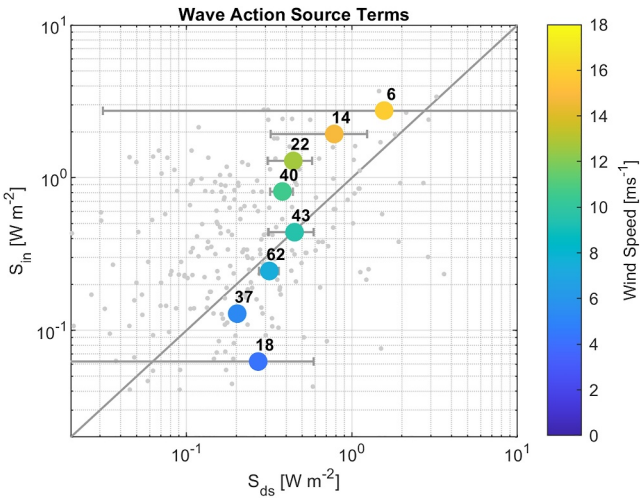


**Figure 9.** Wave action source terms, $S_{in}$ ($y$-axis) and $S_{ds}$ ($x$-axis), colored by wind speed conditions. Individual datapoints are shown in gray, and colored points represent the bin log average for wind speed bins of 2 ms$^{-1}$ width. The number of datapoints in each bin is indicated by the number adjacent to the point. $S_{in}$ shown here is the mean of the four parameterizations presented in Figure 8.

show that breaking dissipation is much less than subsurface dissipation in old seas (wave age > 50). Also shown is the analysis of Banner and Morison (2018), who present the SM15 data as a fraction and fit an exponential curve to the results. Banner and Morison (2018) also force the fit to asymptote at 1 (dashed line) assuming that in young seas, breaking dissipation accounts for all of but not exceed the subsurface dissipation.

The integration of subsurface dissipation has not been treated uniformly in prior experiments. Here, subsurface dissipation derived from the spar buoy is depth integrated, capturing the upper most region of the water column with good agreement with the wind input term (Cifuentes-Lorenzen et al., 2024). The immediate near surface of the water column, above $|z|/H_s < 0.1$ was only partially resolved by the Aquadopp and assumed constant providing good agreement with the wind input term consistent with previous studies (i.e., Terray et al., 1996). SM15 integrate $\epsilon$ to a depth of 20 m; however, they find that total dissipation is not sensitive to the depth of integration but highly sensitive to extrapolation near the surface. This is also the case for Cifuentes-Lorenzen et al. (2024) when exploring the subsurface TKE budget. SM15 cite uncertainties up to an order of magnitude due to the assumed profile of $\epsilon$ between 6 and 12 cm below the surface. Studies using SWIFT buoys integrate $\epsilon$ over approximately 0.5 m below the surface in a wave following reference frame and remove a constant background dissipation of 0.5 Wm$^{-2}$ from the subsurface dissipation estimates. This background dissipation is determined as the dissipation in the absence of breaking waves, thus isolating breaking dissipation from other sources of TKE (Schwendeman et al., 2014; Thomson et al., 2009, 2016).

In young seas, where observations of $S_{ds}$ exceed that of $\epsilon_{spar}$, we hypothesize that a small fraction of $S_{ds}$ is injected by breaking waves to a depth below the depth-integrated estimate of the $\epsilon_{spar}$. However, the SM15 data set integrates $\epsilon$ to a much greater depth (20 m) and nonetheless observe cases where $S_{ds}$ exceeds $\epsilon_{spar}$. Similarly, Cifuentes-Lorenzen et al. (2024) find convergence to LOW around a depth of 6–7 times the significant wave height, suggesting breaking dissipation is confined to the uppermost layer in this data set. In young seas, active breaking could explain cases in which $S_{ds}$ exceeds $\epsilon_{spar}$ due to air-entrainment and bubble injections which contaminate the subsurface signal of the ADCP resulting in $\epsilon_{spar}$ estimates being biased low under particularly strong forcing. In particular, numerical modeling shows that TKE dissipation rates are very high in bubble plumes, and a correction factor for TKE dissipation measurements in conditions of active breaking and high void fraction has been put forward to account for this underestimate (Derakhti et al., 2020). However, without direct observation of TKE dissipation in bubble plumes, this correction factor, based on numerical models, cannot be validated with the present observations. Furthermore, small-scale and micro-scale breakers dominate in young seas and relate to the treatment of $\epsilon$ very close to the surface a region missed by the methods supported by the ADCP. The depth to which dissipation by breaking waves penetrates below the surface has been approximated by length scales defined by the wave amplitude (e.g., Melville et al., 2002). Thus, the subsurface turbulence introduced by microbreakers and small-scale breakers (which accounts for up to 30% of breaking dissipation in this data set) constrained to a depth not resolved by the spar buoy measurements. If breaking-wave dissipation is dominated by small scales in young seas, $\epsilon_{spar}$ may underestimate subsurface dissipation by assuming a constant structure in the wave breaking layer, pointing out the relevance of resolving the structure of the TKE dissipation rate in the uppermost layer.

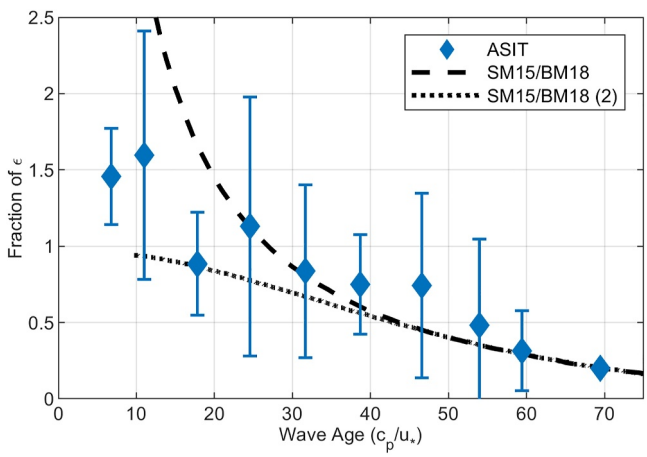


**Figure 10.** The fraction of subsurface dissipation supported by breaking waves ($S_{ds}$) is plotted against wave age Banner and Morison's (2018) analysis of SM15 is shown in black: the dashed line (labeled SM15/BM18) is an exponential fit to the 2,015 data, and the dotted line labeled SM15/BM18 (2) is the same fit forced to asymptote at 1. Standard error is shown on the binned air-sea interaction tower data (blue diamonds).

Figure 10 also shows that in old seas, $S_{ds}$ accounts for only a small fraction of subsurface dissipation. One explanation for this imbalance is a potential bias

in $\epsilon_{spar}$ measurements due to wave orbital shear. The processing of ADCP data to compute $\epsilon_{spar}$ follows methods of previous studies on surface following platforms (Thomson, 2012; Thomson et al., 2016; Wiles et al., 2006; Zippel et al., 2018). Recent work has suggested methods for removing additional bias due to wave orbital shear (Scannell et al., 2017; Zeiden et al., 2023). Preliminary processing of the data found that incorporating the Scannell et al. (2017) correction provided no significant improvement on the "uncorrected" method, which was cross validated with the spectral method of Zippel et al. (2021) and was overall consistent with different observations such as wind input in young seas. If a bias remains, it is likely to be present under old seas. However, given that Sutherland and Melville (2015) observe a similar imbalance in old seas while relying on a substantially different interpolation scheme for $\epsilon(z)$, it is likely that other sources of turbulence are dominant in old seas and drive this observed imbalance.

Other possible sources of turbulence include shear production, buoyancy fluxes, and Langmuir turbulence. Observations of wave action dissipation in the absence of breaking, referred to as swell dissipation, are lacking, and empirical parameterizations of swell dissipation result in dissipation rates orders of magnitude less than observations of breaking dissipation (Schwendeman et al., 2014; Sutherland & Melville, 2015). As noted in Cifuentes-Lorenzen et al. (2024), from a depth-integrated standpoint, shear production and buoyancy terms were second order to dissipation in the TKE budget, highlighting the relevance of the transport terms; however, this claim is primarily based on measurements in young seas. Given that old-seas are wave driven, TKE production due to Stokes drift shear ($\tau \cdot du_s/dz$ where $u_s$ is the Stokes drift) may play a larger role in the TKE budget. Many previous observations have highlighted how Langmuir turbulence and breaking waves are intertwined processes: showing elevated TKE dissipation within bubble plumes beneath the downwelling jets of Langmuir turbulence (Fisher & Nidzieko, 2024; Scully et al., 2015; Zippel et al., 2020). The fraction of subsurface dissipation supported by breaking waves increases with the Langmuir number ($La^2 = u_{*w}/u_s$; e.g. Belcher et al., 2012), indicating that breaking waves account for a smaller percentage of the subsurface dissipation in wave-dominated regime (low-$La$) where Langmuir circulation would likely contribute to subsurface turbulence.

The interaction between nonbreaking waves and subsurface turbulence, including the stretching and compression of vortices by wave orbital motions has been observed to increase vorticity and turbulence related to Langmuir circulations in laboratory and field experiments (Savelyev et al., 2020; Smeltzer et al., 2023; Veron et al., 2009). However, it is hypothesized by Veron et al. (2009) that the orbital motions induced by swell are too weak relative to the subsurface turbulence to have a significant effect on the turbulence. Wave-turbulence interactions, including Langmuir turbulence, remain a possible explanation for an imbalance in $S_{ds}$ and $\epsilon_{spar}$, and field observations of wave-turbulence interactions in the presence of breaking waves should be the focus of future work.

### 4.2. The Relative Role of Small-Scale Breaking Waves

The breaking crest distributions presented here are modified at low speeds to reflect the small and microscale breaking waves that are not captured by the visible imagery. Low crest speed tails are appended to the measured $\Lambda(c)$ distributions to reflect the microbreaking waves that are captured by infrared imagery but not by visible imagery, following the results of Sutherland and Melville (2013). An additional empirical argument for increasing the estimated $\Lambda(c)$ at low speeds comes from a comparison of buoy-mounted visible imagery and shipboard-mounted visible imagery, which finds small-scale whitecaps visible in the higher resolution buoy-mounted imagery but not in the lower resolution shipboard-mounted imagery (Schwendeman et al., 2014). This suggests that the shape of $\Lambda(c)$ at low speeds is also sensitive to image resolution. Additionally, the analysis of Kleiss and Melville (2011) shows that the $\Lambda(c)$ is most sensitive to detection and tracking methods at low speeds. A theoretical case for increasing $\Lambda(c)$ at speeds less than the peak determined by visible imagery is given by Romero et al. (2012): from an equilibrium argument, the inferred shape of the wave energy spectrum at high wavenumbers (low-speeds) indicates that $\Lambda(c)$ should continue to increase at speeds lower than the peak measured by visible imagery. Here, we have presented observations of the wave energy spectrum to very high wavenumbers, and future work should focus on combining such measurements with high resolution, infrared measurements of $\Lambda(c)$ to evaluate Phillips' equilibrium range scaling in spectral estimates of $S_{ds}$ and $S_{in}$.

### 4.3. The Breaking Strength Parameter

The role of small-scale breaking waves and the role of breaking waves in near-surface turbulence have implications for understanding and estimating the breaking strength parameter. First, many prior experiments have

focused on estimating $b_{\text{eff}}$ (Equation 15), equating subsurface TKE dissipation to dissipation by breaking waves. However, as discussed above and as noted previously (Banner & Morison, 2018; Schwendeman et al., 2014; Sutherland & Melville, 2015), observations show a consistent and large imbalance between in $S_{\text{ds}}$ and $\epsilon_{\text{spar}}$ in old seas. All empirical parameterizations of $b_{\text{eff}}$ that use Equation 15 are inherently overestimates because they wrap other sources of TKE dissipation, such as swell dissipation or Langmuir turbulence, into the breaking strength. This imbalance is particularly large in old seas, so the parameterization of Z2016 minimizes this bias by limiting the wave age parametrization of $b_{\text{eff}}$ to wave ages below 50.

The semiempirical model for $b$ defined by R2012, and used in the analysis above, avoids the bias of $b_{\text{eff}}$ by modeling $b$ from a wave action balance perspective, which requires estimating all terms of the wave action equation but avoids making assumptions about sources of subsurface turbulence. Figure 5 shows that $b_{\text{eff}}$ computed from this data set and parameterized by Z2016 overestimate the R2012 model for $b$ computed with measurements of $B(k)$.

In laboratory experiments, the breaking strength parameter has been shown to vary by three orders of magnitude and to increase with wave packet slope (Banner & Peirson, 2007; Drazen et al., 2008; Kendall Melville, 1994). Thus, $b_{\text{eff}}$ as computed in Equation 15 also fails to capture the observed spectral variability of the breaking strength. The R2012 model is a spectral model for $b(k)$, taking into account this variability and computing $b(k)$ as a function of the saturation spectrum, $B(k)$. However, due to the uncertainty in the shape of $\Lambda(c)$ at low speeds, as discussed above, the data used by R2012 are limited to a narrow range of wavenumber ($0.5k_p < k < 8k_p$) in order to minimize bias due to uncertainty in $\Lambda(c)$ and $B(k)$ at small scales. This further emphasizes the need for concurrent measurements of small scale breaking with infrared imagery and measurements of the wave energy spectrum at high wavenumbers.

Moreover, neither treatment of the breaking strength, $b_{\text{eff}}$ derived from subsurface turbulence measurements or $b(k)$ derived from spectral wave measurements, allows for complete fidelity to the scaling arguments of the original laboratory measurements (Duncan, 1981) or scaling arguments (Phillips, 1985). First, $b$ was originally proposed as a numerical constant, such that $S_{\text{ds}}$ scaled as $c^5$, however, as further laboratory observations have shown, $b$ varies by orders of magnitude with wave steepness, implying that $b$ is scale dependent. Additionally, there are no direct field observations of breaking wave dissipation and a scale dependent $b$. Although empirical models of $b(k)$ derived from spectral wave measurements are valuable for wave modeling efforts based on the wave action equation, their direct application to observations of $S_{\text{ds}}$ via $\Lambda(c)$ are not yet addressed. Similar observational constraints apply to parameterizations of $b_{\text{eff}}$. Estimates of $b_{\text{eff}}$ involve averaging of near-surface TKE dissipation rates with highly intermittent instances of wave breaking. Time-averaging subsurface $\epsilon(z)$ measurements result in profiles that are not representative of $\epsilon(z)$ under active breaking, with substantially different profiles of $\epsilon(z)$ under nonbreaking waves. However, utilizing individual measurements of $\epsilon(z)$ under individual actively breaking waves (if bubble contamination can be avoided) would likely show variability with wave steepness and would therefore be best synthesized into a scale-dependent $b(k)$ or $b(c)$ framework with uncertain application to the $S_{\text{ds}} \propto c^5$ scaling.

### 4.4. Energy Transfer and Turbulence in the Wave Boundary Layer

Here, we have used the framework of Duncan (1981) and Phillips (1985) to compute energy dissipation by breaking waves and relate those observations to wave action source terms and the total TKE dissipation in the upper 1.1 m of the ocean. Energy transfer supported by breaking waves also relates to the turbulent structure and the TKE budget in the wave boundary layer of the atmosphere.

Although excess dissipation is observed in the ocean and attributed to an injection of TKE by breaking waves, the wave-induced fluctuations result in an atmospheric $\varepsilon$ deficit when wind energy is going into the wavefield (Cifuentes-Lorenzen et al., 2024; Edson & Fairall, 1998; Janssen, 1999; Liu et al., 2022; Zou et al., 2020). Cifuentes-Lorenzen et al. (2024) present estimates of the energy flux divergence derived from measurements of the TKE dissipation rate on the atmospheric side from the 2019 ASIT TKE campaign. The wave-induced energy transport results in a deficit in measured dissipation ($\epsilon_{\text{obs}}$) relative to the dissipation profile predicted by Monin-Obukhov Similarity Theory as a consequence of an energy flux divergence into the wave field (Janssen, 1999).

Figure 11 compares $S_{\text{ds}}$, $\epsilon$, and $S_{\text{in}}$ with estimates of the energy flux divergence (i.e., $(G_o)$ as presented by Cifuentes-Lorenzen et al. (2024) directly linking the structure of turbulence in the wave-affected layer of the

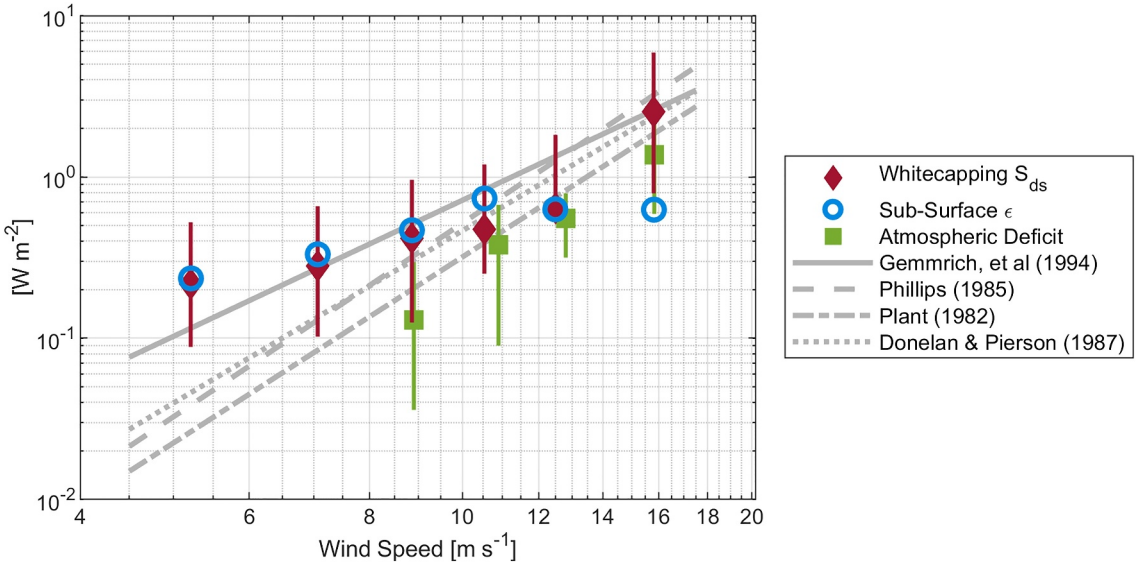


**Figure 11.** Air-sea energy fluxes represented by (1) $S_{ds}$ due to breaking waves, red diamonds, (2) near-surface turbulent kinetic energy (TKE) dissipation, blue circles, (3) the inferred energy transport from the atmospheric TKE budget (integrated TKE dissipation deficit), green squares, and (4) power law fits to observations of $S_{in}$ (as shown in Figure 7), gray lines. Uncertainty bars represent the 95% confidence interval.

atmosphere to energy fluxes through the wave field ($S_{ds}$ and $S_{in}$) and to the excess dissipation observed in the subsurface wave boundary layer. Figure 11 highlights key comparisons between these various measurements of air-sea energy fluxes.

First, estimates of $S_{in}$ from wave spectra are the upper bound of (but within the uncertainty of) energy transport as computed by the atmospheric TKE dissipation rate deficit. Additionally, estimates of $S_{in}$ with wave spectra allow for measurement at low winds, where the deployment configuration does not allow for the capture of the wave-induced signal on the sonic anemometers. Second, as observed in Figure 6, under high winds (>12 ms$^{-1}$), $S_{in}$ exceeds $S_{ds}$. The observations no longer support the assumption of a steady state wave field, and instead it is inferred that $\partial / \partial t\,(E/\omega) > 0$. Under such conditions, we hypothesize that wave growth is occurring, a conclusion consistent with that of Cifuentes-Lorenzen et al. (2024). Third, as highlighted in Figure 7, subsurface dissipation and breaking dissipation approximately balance. At the highest wind speeds, breaking dissipation is greater than subsurface dissipation perhaps due to bubble contamination of subsurface measurements causing underestimate of subsurface dissipation. At low wind speeds, subsurface dissipation is higher than but within the uncertainty of breaking dissipation. These conditions represent the old seas highlighted in Figure 10, where breaking dissipation does not fully account for subsurface dissipation. Last, breaking dissipation and subsurface dissipation are much greater than input in low winds (old seas). This could be due to nonlocal swell advection into the region or nonsteady state conditions where the wavefield energy is decaying and dissipation is outpacing input.

## 5. Conclusions

Observations of breaking wave statistics, wave spectra, and subsurface turbulence measurements were made to evaluate two balances in air-sea energy flux: wave action equilibrium in which breaking wave dissipation balances wind energy input, and the balance by which breaking wave dissipation is responsible for excess TKE dissipation in the near surface ocean. The wave action equilibrium is observed under moderate wind conditions. However, observations at wind speeds above 12 m s$^{-1}$ show an imbalance in which input exceeds dissipation, indicating wave growth. Energy transfer from the atmosphere to the wave field is also inferred from novel observations of the atmospheric TKE dissipation deficit and agree with wind energy input estimates from wave spectra. The near-surface excess TKE dissipation in the ocean is dominated by breaking wave dissipation in young seas, but in old seas, breaking dissipation supports only a small fraction of the near-surface TKE dissipation. In old seas, other sources of TKE dominate and therefore dictate the profile of TKE dissipation. This work highlights both the need for simultaneous observations of small-scale wave breaking and wave height spectra, while also emphasizing that an improved $b(k)$ parameterization would also warrant a renewed examination of the

$c^5$ scaling, particularly in unsteady breaking waves at the sea surface. An ideal observation of $b$ also requires an improved measurement of TKE dissipation under breaking waves, one which is not contaminated by bubbles injected by breaking waves. Furthermore, these observations provide further evidence that breaking waves are a second order source of turbulence to the near-surface ocean in old seas. Observational and numerical process studies should continue to address the mechanisms of turbulence in old seas, including Langmuir turbulence and other wave-turbulence interactions.

## Data Availability Statement

Data used in the study (Zappa & Hogan, 2024) are archived for public access on Columbia Academic Commons (https://doi.org/10.7916/ghvj-kv17).

**Acknowledgments**
This work was supported by NSF Award Number 1756839, ONR Award Number N00014-22-1-2183, and NASA Award Number 80NSSC19K1397. The authors would like to thank the LDEO Field Team, Nathan Laxague, Carson Witte, and Suki Wong, WHOI Engineers, Steve Faluotico, Jay Sisson, and the MVCO Technical Team, Zoe Sandwith, Hugh Popenoe, and Eric Bates. The authors would also like to thank Nathan Laxague and Junzhe Liu for their collaboration in the spectral analysis of the polarimetric imagery.

## References

Agrawal, Y. C., Terray, E. A., Donelan, M. A., Hwang, P. A., Williams, A. J., Drennan, W. M., et al. (1992). Enhanced dissipation of kinetic energy beneath surface waves. *Nature*, *359*(6392), 219–220. https://doi.org/10.1038/359219a0

Banner, M. L., Barthelemy, X., Fedele, F., Allis, M., Benetazzo, A., Dias, F., & Peirson, W. L. (2014). Linking reduced breaking crest speeds to unsteady nonlinear water wave group behavior. *Physical Review Letters*, *112*(11), 114502. https://doi.org/10.1103/PhysRevLett.112.114502

Banner, M. L., & Morison, R. P. (2018). On the upper ocean turbulent dissipation rate due to microscale breakers and small whitecaps. *Ocean Modelling (Oxford)*, *126*, 63–76. https://doi.org/10.1016/j.ocemod.2018.04.004

Banner, M. L., & Peirson, W. L. (2007). Wave breaking onset and strength for two-dimensional deep-water wave groups. *Journal of Fluid Mechanics*, *585*, 93–115. https://doi.org/10.1017/S0022112007006568

Banner, M. L., Zappa, C. J., & Gemmrich, J. R. (2014). A note on the Phillips spectral framework for ocean whitecaps*. *Journal of Physical Oceanography*, *44*(7), 1727–1734. https://doi.org/10.1175/JPO-D-13-0126.1

Belcher, S. E., Grant, A. L. M., Hanley, K. E., Fox-Kemper, B., Van Roekel, L., Sullivan, P. P., et al. (2012). A global perspective on Langmuir turbulence in the ocean surface boundary layer: Frontier. *Geophysical Research Letters*, *39*(18). https://doi.org/10.1029/2012GL052932

Brumer, S. E., Zappa, C. J., Brooks, I. M., Tamura, H., Brown, S. M., Blomquist, B. W., et al. (2017). Whitecap coverage dependence on wind and wave statistics as observed during SO GasEx and HiWinGS. *Journal of Physical Oceanography*, *47*(9), 2211–2235. https://doi.org/10.1175/JPO-D-17-0005.1

Cifuentes-Lorenzen, A., Zappa, C. J., Edson, J. B., O'Donnell, J., & Ullman, D. S. (2024). Exploring the role of wave-driven turbulence at the air-sea interface through measurements of TKE dissipation rates across the interface. *Journal of Geophysical Research: Oceans*. https://doi.org/10.1029/2023JC020308

Craig, P. D., & Banner, M. L. (1994). Modeling wave-enhanced turbulence in the ocean surface layer. *Journal of Physical Oceanography*, *24*(12), 2546–2559. https://doi.org/10.1175/1520-0485(1994)024<2546:MWETIT>2.0.CO;2

Deike, L., & Melville, W. K. (2018). Gas transfer by breaking waves. *Geophysical Research Letters*, *45*(19), 10482–10492. https://doi.org/10.1029/2018GL078758

Derakhti, M., Thomson, J., & Kirby, J. T. (2020). Sparse sampling of intermittent turbulence generated by breaking surface waves. *Journal of Physical Oceanography*, *50*(4), 867–885. https://doi.org/10.1175/JPO-D-19-0138.1

Donelan, M. A., Babanin, A. V., Young, I. R., & Banner, M. L. (2006). Wave-follower field measurements of the wind-input spectral function. Part II: Parameterization of the wind input. *Journal of Physical Oceanography*, *36*(8), 1672–1689. https://doi.org/10.1175/jpo2933.1

Donelan, M. A., & Pierson, W. J. (1987). Radar scattering and equilibrium ranges in wind-generated waves with application to scatterometry. *Journal of Geophysical Research*, *92*(C5), 4971–5029. https://doi.org/10.1029/JC092iC05p04971

Drazen, D. A., Melville, W. K., & Lenain, L. (2008). Inertial scaling of dissipation in unsteady breaking waves. *Journal of Fluid Mechanics*, *611*, 307–332. https://doi.org/10.1017/S0022112008002826

Drennan, W. M., Donelan, M. A., Terray, E. A., & Katsaros, K. B. (1996). Oceanic turbulence dissipation measurements in SWADE. *Journal of Physical Oceanography*, *26*(5), 808–815. https://doi.org/10.1175/1520-0485(1996)026<0808:OTDMIS>2.0.CO;2

Drennan, W. M., Kahma, K. K., Terray, E. A., Donelan, M. A., & Kitaigorodskii, S. A. (1992). Observations of the enhancement of kinetic energy dissipation beneath breaking wind waves. In M. L. Banner & R. H. J. Grimshaw (Eds.), *Breaking waves* (pp. 95–101). Springer Berlin Heidelberg. https://doi.org/10.1007/978-3-642-84847-6_6

Duncan, J. H. (1981). An experimental investigation of breaking waves produced by a towed hydrofoil. *Proceedings of the royal society of London. A. Mathematical and physical sciences* Vol. 377(1770), 331–348. https://doi.org/10.1098/rspa.1981.0127

Eadi Stringari, C., Veras Guimarães, P., Filipot, J.-F., Leckler, F., & Duarte, R. (2021). Deep neural networks for active wave breaking classification. *Scientific Reports*, *11*(1), 3604. https://doi.org/10.1038/s41598-021-83188-y

Edson, J. B., & Fairall, C. W. (1998). Similarity relationships in the marine atmospheric surface layer for terms in the TKE and scalar variance budgets. *Journal of the Atmospheric Sciences*, *55*(13), 2311–2328. https://doi.org/10.1175/1520-0469(1998)055<2311:SRITMA>2.0.CO;2

Fisher, A. W., & Nidzieko, N. J. (2024). AUV observations of Langmuir turbulence in a stratified shelf sea. *Journal of Physical Oceanography*, *54*(9), 1903–1920. https://doi.org/10.1175/JPO-D-23-0136.1

Gemmrich, J. (2010). Strong turbulence in the wave crest region. *Journal of Physical Oceanography*, *40*(3), 583–595. https://doi.org/10.1175/2009JPO4179.1

Gemmrich, J., Zappa, C. J., Banner, M. L., & Morison, R. P. (2013). Wave breaking in developing and mature seas: Breaking crest length distributions. *Journal of Geophysical Research: Oceans*, *118*(9), 4542–4552. https://doi.org/10.1002/jgrc.20334

Gemmrich, J. R., Banner, M. L., & Garrett, C. (2008). Spectrally resolved energy dissipation rate and momentum flux of breaking waves. *Journal of Physical Oceanography*, *38*(6), 1296–1312. https://doi.org/10.1175/2007JPO3762.1

Gemmrich, J. R., & Farmer, D. M. (2004). Near-surface turbulence in the presence of breaking waves. *Journal of Physical Oceanography*, *34*(5), 1067–1086. https://doi.org/10.1175/1520-0485(2004)034<1067:NTITPO>2.0.CO;2

Gemmrich, J. R., Mudge, T. D., & Polonichko, V. D. (1994). On the energy input from wind to surface waves. *Journal of Physical Oceanography*, *24*(11), 2413–2417. https://doi.org/10.1175/1520-0485(1994)024<2413:OTEIFW>2.0.CO;2

Gerbi, G. P., Trowbridge, J. H., Terray, E. A., Plueddemann, A. J., & Kukulka, T. (2009). Observations of turbulence in the ocean surface boundary layer: Energetics and transport. *Journal of Physical Oceanography*, *39*(5), 1077–1096. https://doi.org/10.1175/2008JPO4044.1

Janssen, P. A. E. M. (1999). On the effect of ocean waves on the kinetic energy balance and consequences for the inertial dissipation technique. *Journal of Physical Oceanography*, *29*(3), 530–534. https://doi.org/10.1175/1520-0485(1999)029<0530:OTEOOW>2.0.CO;2

Jessup, A. T., & Phadnis, K. R. (2005). Measurement of the geometric and kinematic properties of microscale breaking waves from infrared imagery using a PIV algorithm. *Measurement Science and Technology*, *16*(10), 1961–1969. https://doi.org/10.1088/0957-0233/16/10/011

Jessup, A. T., Zappa, C. J., Loewen, M. R., & Hesany, V. (1997). Infrared remote sensing of breaking waves. *Nature*, *385*(6611), 52–55. https://doi.org/10.1038/385052a0

Kendall Melville, W. (1994). Energy dissipation by breaking waves. *Journal of Physical Oceanography*, *24*(10), 2041–2049. https://doi.org/10.1175/1520-0485(1994)024<2041:EDBBW>2.0.CO;2

Kleiss, J. M., & Melville, W. K. (2010). Observations of wave breaking kinematics in fetch-limited seas. *Journal of Physical Oceanography*, *40*(12), 2575–2604. https://doi.org/10.1175/2010JPO4383.1

Kleiss, J. M., & Melville, W. K. (2011). The analysis of sea surface imagery for whitecap kinematics. *Journal of Atmospheric and Oceanic Technology*, *28*(2), 219–243. https://doi.org/10.1175/2010JTECHO744.1

Komen, G. J., Cavaleri, L., Donelan, M., Hasselmann, K., Hasselmann, S., & Janssen, P. A. E. M. (1994). *Dynamics and modelling of ocean waves* (1st ed.). Cambridge University Press. https://doi.org/10.1017/CBO9780511628955

Li, Q., & Fox-Kemper, B. (2017). Assessing the effects of Langmuir turbulence on the entrainment buoyancy flux in the ocean surface boundary layer. *Journal of Physical Oceanography*, *47*(12), 2863–2886. https://doi.org/10.1175/JPO-D-17-0085.1

Liu, C., Li, X., Song, J., Zou, Z., Huang, J., Zhang, J. A., et al. (2022). Characteristics of the marine atmospheric boundary layer under the influence of ocean surface waves. *Journal of Physical Oceanography*, *52*(6), 1261–1276. https://doi.org/10.1175/JPO-D-21-0164.1

Melville, W. K., & Matusov, P. (2002). Distribution of breaking waves at the ocean surface. *Nature*, *417*(6884), 58–63. https://doi.org/10.1038/417058a

Melville, W. K., Veron, F., & White, C. J. (2002). The velocity field under breaking waves: Coherent structures and turbulence. *Journal of Fluid Mechanics*, *454*, 203–233. https://doi.org/10.1017/S0022112001007078

Miller, U. K., Zappa, C. J., Zippel, S. F., Farrar, J. T., & Weller, R. A. (2023). Scaling of moored surface ocean turbulence measurements in the southeast pacific ocean. *Journal of Geophysical Research: Oceans*, *128*(1), e2022JC018901. https://doi.org/10.1029/2022JC018901

Mulcahy, J. P., O'Dowd, C. D., Jennings, S. G., & Ceburnis, D. (2008). Significant enhancement of aerosol optical depth in marine air under high wind conditions. *Geophysical Research Letters*, *35*(16), L16810. https://doi.org/10.1029/2008GL034303

Phillips, O. M. (1985). Spectral and statistical properties of the equilibrium range in wind-generated gravity waves. *Journal of Fluid Mechanics*, *156*(1), 505. https://doi.org/10.1017/S0022112085002221

Plant, W. J. (1982). A relationship between wind stress and wave slope. *Journal of Geophysical Research*, *87*(C3), 1961–1967. https://doi.org/10.1029/JC087iC03p01961

Rapp, R. J., & Melville, W. K. (1990). Laboratory measurements of deep-water breaking waves. *Philosophical Transactions of the Royal Society of London - Series A: Mathematical and Physical Sciences*, *331*(1622), 735–800.

Rascle, N., Ardhuin, F., Queffeulou, P., & Croizé-Fillon, D. (2008). A global wave parameter database for geophysical applications. Part 1: Wave-current–turbulence interaction parameters for the open ocean based on traditional parameterizations. *Ocean Modelling (Oxford)*, *25*(3–4), 154–171. https://doi.org/10.1016/j.ocemod.2008.07.006

Romero, L. (2019). Distribution of surface wave breaking fronts. *Geophysical Research Letters*, *46*(17–18), 10463–10474. https://doi.org/10.1029/2019GL083408

Romero, L., Melville, W. K., & Kleiss, J. M. (2012). Spectral energy dissipation due to surface wave breaking. *Journal of Physical Oceanography*, *42*(9), 1421–1444. https://doi.org/10.1175/JPO-D-11-072.1

Sallée, J.-B., Shuckburgh, E., Bruneau, N., Meijers, A. J. S., Bracegirdle, T. J., & Wang, Z. (2013). Assessment of Southern Ocean mixed-layer depths in CMIP5 models: Historical bias and forcing response. *Journal of Geophysical Research: Oceans*, *118*(4), 1845–1862. https://doi.org/10.1002/jgrc.20157

Savelyev, I. B., Buckley, M. P., & Haus, B. K. (2020). The impact of nonbreaking waves on wind-driven ocean surface turbulence. *Journal of Geophysical Research: Oceans*, *125*(1), e2019JC015573. https://doi.org/10.1029/2019JC015573

Scannell, B. D., Rippeth, T. P., Simpson, J. H., Polton, J. A., & Hopkins, J. E. (2017). Correcting surface wave bias in structure function estimates of turbulent kinetic energy dissipation rate. *Journal of Atmospheric and Oceanic Technology*, *34*(10), 2257–2273. https://doi.org/10.1175/JTECH-D-17-0059.1

Schwendeman, M., & Thomson, J. (2015). Observations of whitecap coverage and the relation to wind stress, wave slope, and turbulent dissipation. *Journal of Geophysical Research: Oceans*, *120*(12), 8346–8363. https://doi.org/10.1002/2015JC011196

Schwendeman, M., Thomson, J., & Gemmrich, J. R. (2014). Wave breaking dissipation in a young wind sea. *Journal of Physical Oceanography*, *44*(1), 104–127. https://doi.org/10.1175/JPO-D-12-0237.1

Scully, M. E., Fisher, A. W., Suttles, S. E., Sanford, L. P., & Boicourt, W. C. (2015). Characterization and modulation of Langmuir circulation in Chesapeake bay. *Journal of Physical Oceanography*, *45*(10), 2621–2639. https://doi.org/10.1175/JPO-D-14-0239.1

Scully, M. E., Trowbridge, J. H., & Fisher, A. W. (2016). Observations of the transfer of energy and momentum to the oceanic surface boundary layer beneath breaking waves. *Journal of Physical Oceanography*, *46*(6), 1823–1837. https://doi.org/10.1175/JPO-D-15-0165.1

Scully, M. E., & Zippel, S. F. (2024). Vertical energy fluxes driven by the interaction between wave groups and Langmuir turbulence. *Journal of Physical Oceanography*, *54*(7), 1347–1366. https://doi.org/10.1175/JPO-D-23-0193.1

Smeltzer, B. K., Rømcke, O., Hearst, R. J., & Ellingsen, S. Å. (2023). Experimental study of the mutual interactions between waves and tailored turbulence. *Journal of Fluid Mechanics*, *962*, R1. https://doi.org/10.1017/jfm.2023.280

Stansell, P., & MacFarlane, C. (2002). Experimental investigation of wave breaking criteria based on wave phase speeds. *Journal of Physical Oceanography*, *32*(5), 1269–1283. https://doi.org/10.1175/1520-0485(2002)032<1269:EIOWBC>2.0.CO;2

Sutherland, G., Ward, B., & Christensen, K. H. (2013). Wave-turbulence scaling in the ocean mixed layer. *Ocean Science*, *9*(4), 597–608. https://doi.org/10.5194/os-9-597-2013

Sutherland, P., & Melville, W. K. (2013). Field measurements and scaling of ocean surface wave-breaking statistics: Surface wave-breaking statistics. *Geophysical Research Letters*, *40*(12), 3074–3079. https://doi.org/10.1002/grl.50584

Sutherland, P., & Melville, W. K. (2015). Field measurements of surface and near-surface turbulence in the presence of breaking waves. *Journal of Physical Oceanography*, *45*(4), 943–965. https://doi.org/10.1175/JPO-D-14-0133.1

Terray, E. A., Donelan, M. A., Agrawal, Y. C., Drennen, W. M., Kahma, K. K., Williams, A. J., et al. (1996). Estimates of kinetic energy dissipation under breaking waves. *Journal of Physical Oceanography*, *26*(5), 792–807. https://doi.org/10.1175/1520-0485(1996)026<0792:EOKEDU>2.0.CO;2

Thomson, J. (2012). Wave breaking dissipation observed with "SWIFT" drifters. *Journal of Atmospheric and Oceanic Technology*, *29*(12), 1866–1882. https://doi.org/10.1175/JTECH-D-12-00018.1

Thomson, J., Gemmrich, J. R., & Jessup, A. T. (2009). Energy dissipation and the spectral distribution of whitecaps. *Geophysical Research Letters*, *36*(11), L11601. https://doi.org/10.1029/2009GL038201

Thomson, J., & Jessup, A. T. (2009). A Fourier-based method for the distribution of breaking crests from video observations. *Journal of Atmospheric and Oceanic Technology*, *26*(8), 1663–1671. https://doi.org/10.1175/2009JTECHO622.1

Thomson, J., Schwendeman, M. S., Zippel, S. F., Moghimi, S., Gemmrich, J., & Rogers, W. E. (2016). Wave-breaking turbulence in the ocean surface layer. *Journal of Physical Oceanography*, *46*(6), 1857–1870. https://doi.org/10.1175/JPO-D-15-0130.1

Ticona Rollano, F., Brown, A., Ellenson, A., Özkan-Haller, H. T., Thomson, J., & Haller, M. C. (2019). Breaking waves in deep water: Measurements and modeling of energy dissipation. *Ocean Dynamics*, *69*(10), 1165–1179. https://doi.org/10.1007/s10236-019-01301-2

Toba, Y., & Kawamura, H. (1996). Wind-wave coupled downward-bursting boundary layer (DBBL) beneath the sea surface. *Journal of Oceanography*, *52*(4), 409–419. https://doi.org/10.1007/BF02239046

Veron, F. (2015). Ocean spray. *Annual Review of Fluid Mechanics*, *47*(1), 507–538. https://doi.org/10.1146/annurev-fluid-010814-014651

Veron, F., Melville, W. K., & Lenain, L. (2009). Measurements of ocean surface turbulence and wave–turbulence interactions. *Journal of Physical Oceanography*, *39*(9), 2310–2323. https://doi.org/10.1175/2009JPO4019.1

VreĆica, T., Pizzo, N., & Lenain, L. (2022). Observations of strongly modulated surface wave and wave breaking statistics at a submesoscale front. *Journal of Physical Oceanography*, *52*(2), 289–304. https://doi.org/10.1175/JPO-D-21-0125.1

Wiles, P. J., Rippeth, T. P., Simpson, J. H., & Hendricks, P. J. (2006). A novel technique for measuring the rate of turbulent dissipation in the marine environment. *Geophysical Research Letters*, *33*(21), L21608. https://doi.org/10.1029/2006GL027050

Wu, J., Popinet, S., & Deike, L. (2023). Breaking wave field statistics with a multi-layer model. *Journal of Fluid Mechanics*, *968*, A12. https://doi.org/10.1017/jfm.2023.522

Wunsch, C. (2020). Is the ocean speeding up? Ocean surface energy trends. *Journal of Physical Oceanography*, *50*(11), 3205–3217. https://doi.org/10.1175/JPO-D-20-0082.1

Zappa, C. J., Asher, W. E., & Jessup, A. T. (2001). Microscale wave breaking and air-water gas transfer. *Journal of Geophysical Research*, *106*(C5), 9385–9391. https://doi.org/10.1029/2000JC000262

Zappa, C. J., Banner, M. L., Morison, R. P., & Brumer, S. E. (2016). On the variation of the effective breaking strength in oceanic sea states. *Journal of Physical Oceanography*, *46*(7), 2049–2061. https://doi.org/10.1175/JPO-D-15-0227.1

Zappa, C. J., Banner, M. L., Schultz, H., Corrada-Emmanuel, A., Wolff, L. B., & Yalcin, J. (2008). Retrieval of short ocean wave slope using polarimetric imaging. *Measurement Science and Technology*, *19*(5), 055503. https://doi.org/10.1088/0957-0233/19/5/055503

Zappa, C. J., & Hogan, L. (2024). Data for: Observations of breaking wave dissipation and their relationship to Atmosphere-Ocean Energy transfer v1 [Dataset]. *Columbia Academic Commons*. https://doi.org/10.7916/ghvj-kv17

Zappa, C. J., McGillis, W. R., Raymond, P. A., Edson, J. B., Hintsa, E. J., Zemmelink, H. J., et al. (2007). Environmental turbulent mixing controls on air-water gas exchange in marine and aquatic systems. *Geophysical Research Letters*, *34*(10). https://doi.org/10.1029/2006GL028790

Zappa, C. J., Raymond, P. A., Terray, E. A., & McGillis, W. R. (2003). Variation in surface turbulence and the gas transfer velocity over a tidal cycle in a macro-tidal estuary. *Estuaries*, *26*(6), 1401–1415. https://doi.org/10.1007/BF02803649

Zeiden, K., Thomson, J., & Girton, J. (2023). Estimating profiles of dissipation rate in the upper ocean using acoustic Doppler measurements made from surface-following platforms. *Journal of Atmospheric and Oceanic Technology*, *40*(12), 1383–1401. https://doi.org/10.1175/JTECH-D-23-0027.1

Zippel, S. F., Farrar, J. T., Zappa, C. J., Miller, U., Laurent, L. S., Ijichi, T., et al. (2021). Moored turbulence measurements using pulse-coherent Doppler sonar. *Journal of Atmospheric and Oceanic Technology*, *38*(9), 1621–1639. https://doi.org/10.1175/JTECH-D-21-0005.1

Zippel, S. F., Maksym, T., Scully, M., Sutherland, P., & Dumont, D. (2020). Measurements of enhanced near-surface turbulence under windrows. *Journal of Physical Oceanography*, *50*(1), 197–215. https://doi.org/10.1175/JPO-D-18-0265.1

Zippel, S. F., Thomson, J., & Farquharson, G. (2018). Turbulence from breaking surface waves at a river mouth. *Journal of Physical Oceanography*, *48*(2), 435–453. https://doi.org/10.1175/JPO-D-17-0122.1

Zou, Z., Li, S., Huang, J., Li, P., Song, J., Zhang, J. A., & Wan, Z. (2020). Atmospheric boundary layer turbulence in the presence of swell: Turbulent kinetic energy budget, Monin–Obukhov similarity theory, and inertial dissipation method. *Journal of Physical Oceanography*, *50*(5), 1213–1225. https://doi.org/10.1175/JPO-D-19-0136.1